Hydrogen Peroxide Synthesis on Porous Graphitic Carbon Nitride Using Water as Hydrogen Source

Journal:	*Journal of Materials Chemistry A*
Manuscript ID	TA-ART-07-2019-008103.R2
Article Type:	Paper
Date Submitted by the Author:	14-Oct-2019
Complete List of Authors:	Cao, Yongyong; Zhejiang University of Technology Zhou, Guobing ; University of Oklahoma Chen, Xianlang; Zhejiang University of Technology Qiao, Qi; University of Oklahoma Zhao, Chenxia; Zhejiang University of Technology Sun, Xiang; Zhejiang University of Technology Zhong, Xing; Zhejiang University of Technology Zhuang, Gui-lin; Zhejiang University of Technology Deng , Shengwei; Zhejiang University of Technology Wei, Zhongzhe; Zhejiang University of Technology Yao, Zihao; Zhejiang University of Technology, College of Chemical Engineering Huang, Liangliang; University of Oklahoma Wang, Jian-guo; Zhejiang University of Technology

SCHOLARONE™
Manuscripts

Hydrogen Peroxide Synthesis on Porous Graphitic Carbon Nitride Using Water as Hydrogen Source

Yongyong Cao[1], Guobing Zhou[2], Xianlang Chen[1], Qi Qiao[2], Chenxia Zhao[1], Xiang Sun[1]. Xing Zhong[1],

Guilin Zhuang[1], Shengwei Deng[1], Zhongzhe Wei[1], Zihao Yao[1], Liangliang Huang[*2], Jianguo Wang[*1]

1. Institute of Industrial Catalysis, College of Chemical Engineering, State Key Laboratory Breeding Base of Green-Chemical Synthesis Technology, Zhejiang University of Technology, Hangzhou 310032 China

2. School of Chemical, Biological and Materials Engineering, University of Oklahoma, Norman, Oklahoma 73019, United States

Abstract: Using water as hydrogen source is a promising strategy for alternative hydrogen peroxide (H_2O_2) synthesis. By a series of *ab initio* molecular dynamics (AIMD) simulations and reactive molecular dynamics (RxMD) calculations, fundamental details have been revealed regarding how liquid water interat with oxygen on a metal-free carbon nitride catalyst, and the two-step reaction mechanism of H_2O_2 synthesis. The metal-free porous graphitic carbon nitride ($g\text{-}C_5N_2$) catalysts are also systematically screened by a thermodynamics approach through *ab initio* density functional theory

* Corresponding authors. Email: HLL@ou.edu (Liangliang Huang); jgw@zjut.edu.cn (Jianguo Wang)

(DFT) method. Key results include: (a) a pristine g-C_5N_2 is most active to catalyze H_2O/O_2 reaction and produce H_2O_2; (b) the adsorption and activation of water at unsaturated carbon sites of g-C_5N_2 is critical to initiate the H_2O/O_2 reaction, producing HOO* intermediates; (c) interfacial free water and adsorbed water at g-C_5N_2 form a synergetic proton transfer cluster to promote HOO* intermediates to H_2O_2. To the best of our knowledge, this work presents long-needed theoretical details of direct H_2O_2 synthesis via the water/oxygen system, which can guide further optimizations of carbon-based catalysts for oxygen reduction reactions.

Keywords: H_2O_2 synthesis, graphitic carbon nitride, oxygen reduction, proton transfer, molecular dynamics simulation

1. Introduction

Hydrogen peroxide (H_2O_2) has been extensively used for pulp bleaching, wastewater treatment and green oxidizations for chemical syntheses[1-3]. With the increasing global demand, how to synthesize H_2O_2 via economic and environment friendly processes is a pressing topic. Currently, over 95% of H_2O_2 is produced using an indirect process, involving energy-intensive multistep anthraquinone oxidation and reduction reactions[1, 4]. The industrialized process requires a complex and large-scale infrastructure and produces severe pollution to the environment due to the utilization of aromatic chemicals[5]. Since last decade, direct synthesis of H_2O_2 via the two-proton hydrogen/oxygen reaction has attracted much attention[6, 7]. Various metal and metal oxide catalysts have been proposed

and optimized, among which Pd based alloys and nanoparticles seem to be most promising[8-11]. Unfortunately, this method is limited by the heavy use of strong acid and halide, which would promote metal catalyst leaching and as-produced H_2O_2 requires a further purification[8]. In addition, the hydrogen explosion risk at the operational high pressure continues to be a safety hazard and prevents the commercial scale implementation[12].

Direct H_2O_2 synthesis at ambient conditions, utilizing water as hydrogen resources and combining electrocatalysis or photocatalysis techniques, has been witnessing tremendous research efforts recently[13-17]. Shunichi et al[18] prepared a Fe-Ru bifunctional catalyst to produce H_2O_2 from H_2O and O_2 via visible-light photocatalytic reactions. They observed that H_2O adsorption on Fe sites is critical to the following O_2/H_2O reaction. Electrochemically, H_2O_2 synthesis from H_2O and O_2 is a typical two-proton/two-electron ($2H^+/2e^-$) oxygen reduction reaction (ORR)[19]. A number of catalysts have been developed with promising efficiency for electrochemical ORR processes, including noble metal-based electrocatalysts (Au[20], Pt[21] and Pd[17]), single-atom catalyst (Pt@TiN[22]), metal oxides catalysts (Fe_3O_4[23], Mn-Ru oxide[24]) and carbon-based electrocatalysts (N-doped, or B, N co-doped mesoporous carbon[25-28]).

Carbon-based catalysts have been considered as an efficient low-cost, metal-free alternative for green and renewable processes[29-33]. For H_2O_2 synthesis from H_2O and O_2, Cui et al [34] reported that oxidized carbon nanotubes (CNT) exhibited a higher selectivity and a better activity for the two-electron oxygen reduction reaction. Yang and co-workers[35] found that epoxy and ring ether groups of graphene oxide exhibit an outstanding electrochemical HO_2^- production, achieving a good activity (overpotential <10 mV), an excellent selectivity($\approx$100%) and a satisfactory stability (over 15 h at 0.45

V in the alkaline media). Despite those encouraging progress of carbon-based catalysts for direct H_2O_2 synthesis, detailed fundamental understandings are still incomplete. To just name a few, what is the exact catalytic role of carbon-based material? What is the critical initial step to H_2O_2 synthesis, water adsorption or oxygen interaction with the catalyst? Is it a one-step reaction, or a subsequent two-step proton/electron reaction mechanism? What is the role of the liquid/solid interface?

In this work we report a computational study to reveal the reaction mechanism of how to directly synthesize H_2O_2 by H_2O/O_2 reaction on a porous graphitic carbon nitride (g-C_5N_2). Also known as Aza-fused π-conjugated microporous polymer (Aza-CMP), g-C_5N_2 has a high number of pyridinic nitrogen dopants at zigzag edges, a large surface area, a high pore/volume ratio, and a high electrical conductivity[36-38]. Through a series of AIMD, RxMD and *ab initio* DFT calculations, the following key results have been elucidated: (a) pristine and hydrogenated g-C_5N_2 catalysts have been screened and the most effective catalyst is a partially hydrogenated metastable g-C_5N_2. (b) positively charged carbon sites preferentially chemisorb water molecules, which is critical to promote the H_2O/O_2 intraction and generate HOO* intermediates towards H_2O_2 production. (c) a collection of near-surface water molecules could form a proton transfer chain, thus conveniently promoting the reaction of HOO* intermediate to H_2O_2.

2. Models and Simulation Methods

2.1 ReaxFF based Reactive Molecular Dynamics Simulation

Developed by van Duin and co-workers, ReaxFF force field provides affordable and accurate atomic details of reactive complex systems[39, 40]. With a bond order concept, ReaxFF force field parameters have been fitted to reproduce *ab initio* quantum mechanics calculations. Therefore, ReaxFF based reactive molecular dynamics (RxMD) simulations can describe reacting systems with a similar accuracy to *ab initio* quantum mechanics methods, and effectively handle systems of hundreds of thousands of molecules. The C/N/O/H ReaxFF force field parameters in this work are extracted from the literature[41]. Structural information of g-C_5N_2 has been calculated by both RxMD and ab initio DFT calculations. As presented in Fig S1, the results of characteristic bonds and angles agree quantitatively well with each other. It is also worth noting that RxMD simulations were tested where only 500 water and 25 oxygen molecules were placed in the simulation box at 300.0 K. The simulation results indicated that this process was only a simple physical mix, no OOH* and H_2O_2 can be observed after 5 ns (Fig. S2). RxMD simulations were performed with the LAMMPS software package[42]. The canonical ensemble was applied where the number of molecules (N), the volume (V), and the temperature (T) hold constant throughout the calculations. The temperature (300.0 K) was maintained by the Nosé-Hoover method with the damping coefficient of 100.0 fs[43, 44]. Initial velocities of water and oxygen molecules were assigned according to the Boltzmann distribution. The g-C_5N_2 was treated as a flexible solid substrate during the calculation. The Newton's equation was integrated by the velocity Verlet algorithm with a time step of 0.25 fs[45]. A bond-order change of 20% of the original bond length was used to identify the connectivity and molecular species, and monitor the system evolution as a function of simulation time.

As illustrated in Fig. 1a, a 2 × 2 supercell was constructed based on the optimized primitive unit

cell of g-C$_5$N$_2$ containing 30 C and 12 N atoms. The simulation box was composed of a single sheet

of g-C$_5$N$_2$, 68.98 Å (y) × 57.71 Å (x), placed in the middle, and a mixture of 500 water molecules

and 25 oxygen molecules, as shown in Fig. 1b. The z dimension of the simulation box was 30.0 Å, so

that the interaction between neighboring g-C$_5$N$_2$ sheets is negligible. Periodic boundary conditions

were applied along the x, y, and z directions. For each RxMD simulation, the system (water, oxygen

and g-C$_5$N$_2$) was firstly relaxed to optimize the structures, followed by a 2.0 ns calculation to further

equilibrate the system. After that, the data was collected for 200 ps for analysis. It is worth noting that

there was no restriction on the system: both g-C$_5$N$_2$, water and oxygen molecules were allowed to relax
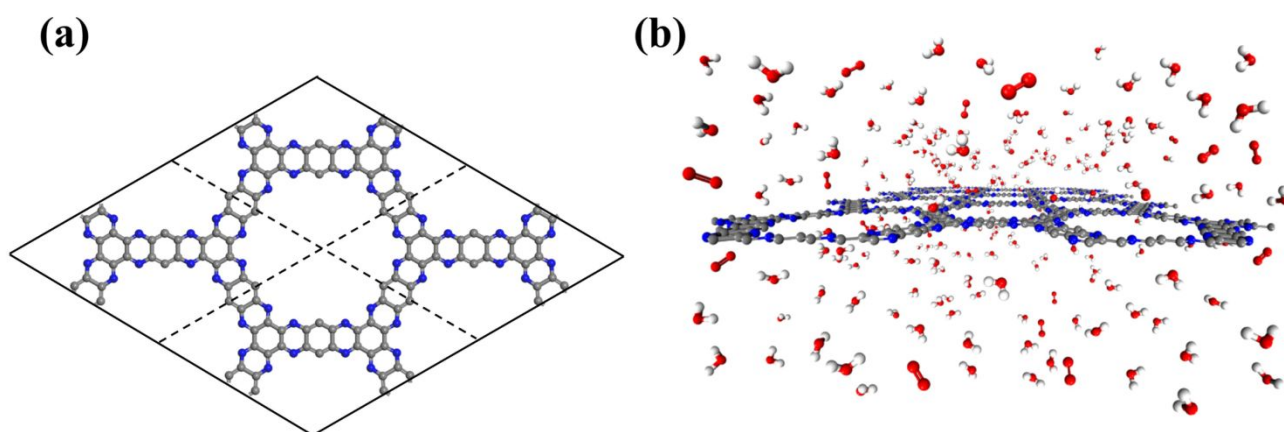
and move during the simulation.

Fig. 1 The illustrations of (a) initial configurations of a 2 × 2 g-C$_5$N$_2$ supercell. (b) the simulation box

of g-C$_5$N$_2$, H$_2$O and O$_2$ molecules.

2.2 *Ab initio* DFT and *ab initio* MD Calculations

Three sets of *ab initio* quantum mechanics calculations have been performed to: (I) screen and evaluate structural stability of pristine and hydrogenated g-C_5N_2 models; (II) search and reveal H_2O/O_2 reaction mechanism details, such as the transition state, the reaction pathway and the activation energy barrier; (III) generate the reaction trajectory and dynamics properties, to compare with RxMD calculation results, and to identify the two-proton/two-electron ($2H^+/2e^-$) reaction process.

Geometry optimization and transition state calculation were performed by the *ab initio* DFT method via the Vienna *ab initio* simulation package (VASP)[46-48]. The exchange-correlation functional was treated via the generalized gradient approximation (GGA) method with Perdew-Burke-Ernzerhof (PBE)[49]. The empirical D3 Grimme's method (DFT-D3) was adopted to improve the description of van der Waals interactions in all calculations[50]. The planewave kinetic energy cutoff was 450.0 eV. Geometries were optimized until the residual forces were smaller than 0.05 eV/Å. A 5×5×1 grid was used for k–point sampling, according to the Monkhorst-Pack method[51]. A vacuum of 20.0 Å was added to the z direction to avoid mirror image interactions. Climbing image-modified nudged elastic band (CI-NEB) method was used to evaluate activation energies of different reaction paths[52]. A total of 55 g-C_5N_2 models were generated to represent pristine and all possible hydrogenations in terms of coverage and distribution of hydrogen atoms. Optimized structures and corresponding equilibrium energies are summarized in Fig. S3 and Table S1 of the supplementary material.

Ab initio molecular dynamics (AIMD) calculations were performed by the CP2K package[49, 53]. The system (g-C_5N_2, water and oxygen) was maintained at 300.0 K using the canonical (NVT)

ensemble, where the temperature was controlled via the Nosé-Hoover thermostat[43, 54]. Each calculation was studied for 2.0 ps with a time step of 0.25 fs. The wave functions were expanded in an optimized double-ζ Gaussian basis set[55]. The electrostatic energy cutoff for an auxiliary plane wave basis set was 360.0 Ry[56]. Van der Waals interactions were corrected by the Grimme algorithm (DFT-D3)[50].

2.3 Choice of Three Simulation Methods

While the overall goal of this work is to reveal how water and oxygen react on a carbon nitride catalyst (g-C_5N_2) to produce hydrogen peroxide, it is worth to explore for thermal stability of catalyst and the diffusion/reaction coupled complex process. Thus, we take advantages of three adopted simulation methods to understand the system. First of all, to mimic experimental g-C_5N_2 and provide insight to catalyst screening and optimization, a series of *ab initio* DFT were performed to calculate Gibbs free energy and evaluate thermal stability of all g-C_5N_2 models. Secondly, it is critical to understand the first step of the reaction, the energy barrier and reaction pathway. Thus, *ab initio* quantum mechanics methods are proper choices. Along this direction, we have performed ab initio DFT and AIMD calculations. Thirdly, H_2O_2 synthesis is a complex system and it happens at the gas/liquid/solid interface. Obviously, the adsorption and diffusion of reactants (H_2O and O_2) to the solid interface (g-C_5N_2) could be significant parameters. Additionally, after the synthesis reaction, the competitive desorption of H_2O_2 from the solid interface is also vital to a successful separation and purification of H_2O_2 product. ReaxFF potential has become a powerful computational tool to explore, chemisorption and reactions of complex systems. More importantly, RxMD simulations not only can describe systems composed of hundreds of thousands of atoms but can archive a trajectory to the time

8

sale of microseconds. Therefore, RxMD was adopted to study such a complex and multiscale system. The three methods compensate each other and provide insights from different perspectives.

3. Results and Discussions

3.1 Gibbs Free Energy Calculation and Thermal Stability of g-C_5N_2 Models

The stability of 55 g-C_5N_2 models was firstly investigated by the *ab initio* DFT based thermodynamics approach[57-59]. The most stable model generally has the lowest Gibbs free energy. In this work, the surface energy (Ω) is calculated according to eqn.[60, 61] (1):

$$\Omega(T,P_i, N_i) = \frac{1}{2A}\big(G(T,P_i, N_i) - \sum_i N_i\mu_i(T,P_i)\big) \tag{1}$$

where A and G are surface area and Gibbs free energy of the g-C_5N_2 model, respectively; μ_i is overall chemical potential of a total number of N_i atoms or molecules of species *i*. *T* is temperature; *P* is hydrogen partial pressure. For solid phase, the change of *P* has negligible effect on the Ω value. Thus, eqn. (1) could be expressed as:

$$\Omega(T,P_i, N_i) = \frac{1}{2A}\big(E_{g\_C_5N_2\_H} - E_{g\_C_5N_2} - N_H\mu_H\big) \tag{2}$$

where $E_{g\_C_5N_2\_H}$ and $E_{g\_C_5N_2}$ are respectively the total energy of hydrogenated g-C_5N_2 and pristine g-C_5N_2 from *ab initio* DFT calculations; N_H is the number of hydrogen atoms of the g-C_5N_2 model; μ_H is the chemical potential of a single hydrogen atom, which is approximated by the chemical potential of a gas-phase hydrogen molecule:

$$\mu_H = \frac{\mu_{H_2}^{gas}}{2} \tag{3}$$

At the studied temperature of 300.0 K, the gas-phase hydrogen could be treated as ideal gas.

Therefore, the chemical potential could be calculated by eqn. (4):

$$\mu_{H_2}^{gas}(T,P_{H_2}) = \mu_{H_2}^{gas}(T,P^0) + kT\ln\left(\frac{P_{H_2}}{P^0}\right)$$

$$= \mu_{H_2}^{gas}(T^0,P^0) + \Delta G_{H_2}^{gas}(T,P^0) + kT\ln\left(\frac{P_{H_2}}{P^0}\right) \tag{4}$$

where $\mu_{H_2}^{gas}(T^0,P^0)$ is the chemical potential of hydrogen molecule at the standard state ($T^0 = 298.15$

K, $P^0 = 1$ atm), $kT\ln\left(\frac{P_{H_2}}{P^0}\right)$ is the pressure-dependent term. $\Delta G_{H_2}^{gas}(T,P^0)$ is the temperature-dependent

term, referring to the Gibbs free energy change when the temperature changes from $T^0 = 298.15$ K to

$T = 300.0$ K (see Table S2), while keeping the pressure at P^0:

$$\Delta G_{H_2}^{gas}(T,P^0) = G_{H_2}^{gas}(T,P^0) - G_{H_2}^{gas}(T^0,P^0) \tag{5}$$

The chemical potential of hydrogen molecule at standard state condition is from:

$$\mu_{H_2}^{gas}(T^0,P^0) = H_{H_2}^0 - T^0 S_{H_2}^0 \tag{6}$$

where $S_{H_2}^0$ is from the NIST thermodynamic tables[62], and $H_{H_2}^0$ is calculated using experimental data

of heat of formation of water:

$$H_{H_2}^0 = H_{H_2O}^0 - \frac{1}{2}H_{O_2}^0 - \Delta H_{f,H_2O}^0 \tag{7}$$

where the enthalpies of $H_{O_2}^0$ and $H_{H_2O}^0$ are adopted from the literatures. The oxygen gas entropy $S_{O_2}^0$

at the standard state is from experimental data. Hence, eqns. (2) and (3) yield:

$$\mu_H = 0.5[H_{H_2O}^0 - \frac{1}{2}H_{O_2}^0 - \Delta H_{f,H_2O}^0 + \Delta G_{H_2}^{gas}(T,P^0) + kT\ln(\frac{P_{H_2}}{P^0}) \tag{8}$$

$$\Omega(T, P_i, N_i) = \frac{1}{2A}\{E_{C_5N_{2H}} - E_{C_5N_{2\_H}} - 0.5N_H$$

$$\left[H^0_{H_2O} - \frac{1}{2}H^0_{O_2} - \Delta H^0_{f,H_2O} + \qquad \Delta G^{gas}_{H_2}(T,P^0) + kT\ln\left(\frac{P_{H_2}}{P^0}\right)\right]\}$$

(9)

As shown in Fig. S3 and Table S1, the proposed models are constructed by the degree of hydrogenation, that is, the number of hydrogen atoms added to the pristine g-C_5N_2. When multiple candidates exist for a same degree of hydrogenation, the most stable model (with the lowest Gibbs free energy) is then selected as the representative one. With this information, 19 out of the total 55 possible g-C_5N_2 models were selected for the Gibbs free energy calculation to evaluate their thermo stability. The calculations were performed under the atmosphere condition, as a function of variation of hydrogen chemical potential from -0.58 eV to -1.10 eV, which corresponds to the temperature range of 300.0 to 1100.0 K. As shown in Fig. 2a, the Gibbs free energy was expressed as a function of temperature at a fixed partial pressure of hydrogen, P_{H_2} = 1atm. A more negative Gibbs free energy indicates a better thermo stability of the g-C_5N_2 model. In addition, the negative slope suggests that the thermo stability generally declines when temperature increases. According to the Gibbs free energy calculation, the hydrogen coverage (i.e., the degree of hydrogenation) affects the thermo stability. But the dependence is not linear according to the results in Fig. 2a. This is probably due to different activities of C and N sites of g-C_5N_2. A same degree of hydrogenation could have different hydrogen distributions from C and N sites.
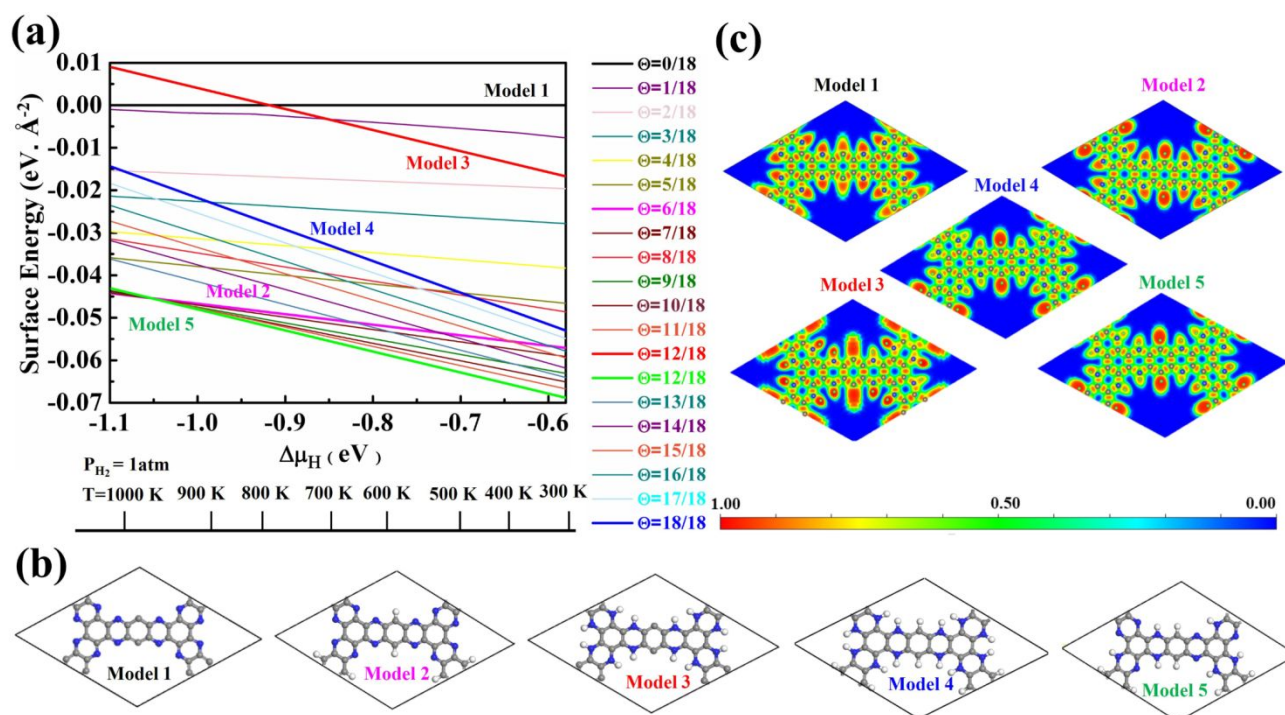
11

Fig. 2 Calculations of thermodynamic stability and electron structure. (a) Phase diagrams: the regions of stability of g-C_5N_2 surfaces with different terminations as a function of hydrogen chemical potential variations. (b) Five selected model structures of g-C_5N_2. (c) Electronic localized function (ELF) analysis to the five models. For the scale bar of 0.0 to 1.0, the red region indicates a higher local electron distribution, the green region represents electronic-gas-like pair probability and the blue region shows a higher electronic delocalized distribution.

In this work, we selected five models to study their catalytic roles to H_2O_2 synthesis. As illustrated in Fig. 2b, the models represent respectively pristine (Model 1, no hydrogenation), C-site full hydrogenation (Model 2), N-site full hydrogenation (Model 3), full hydrogenation (Model 4, both C and N sites hydrogenated), and partially hydrogenation (Model 5, C sites fully, N sites partially hydrogenated), which is the most stable model from the Gibbs free energy calculation. The electron

localization function (ELF) analysis of Fig. 2c shows the distribution of electrons of the models, where

sites with higher electron densities (red color) are preferential to interact with H_2O and O_2 molecules.

3.2 Preferential Water Adsorption on g-C_5N_2

In order to elucidate which reactant (H_2O or O_2) initiates the reaction, the H_2O/g-C_5N_2 and O_2/g-

C_5N_2 systems have been studied separately with the pristine Model 1. *Ab initio* DFT calculations reveal

that O_2 and H_2O adsorption at the pore of g-C_5N_2 has stronger binding energies than that of the basal

plane of g-C_5N_2 (Fig. S4). The adsorption energy is respectively -1.68 eV and -1.14 eV for H_2O/g-

C_5N_2 and O_2/g-C_5N_2 at the unsaturated C site, suggesting a preferential interaction between H_2O and

g-C_5N_2. The comparison was performed from RxMD simulations where 500 H_2O molecules or 50 O_2

molecules were placed to interact with the pristine g-C_5N_2 (Model 1) at 300.0 K. For the O_2/g-C_5N_2

system, only 4 O_2 molecule adsorbed at unsaturated C sites. No preferential interaction between O_2/N

sites was observed, see Fig. S5 of the supplementary material. Meanwhile, for the H_2O/g-C_5N_2 system,

as Fig. 3a shows, water preferentially distributed to form an ordered ring configuration along the pores

of pristine g-C_5N_2. This phenomenon was also observed via ab initio DFT calculation. A zoom-in

snapshot of Fig. 3b clearly reveals three types of water molecules in the system, namely, adsorbed

water at unsaturated C sites, water molecules near g-C_5N_2 which form a hydrogen bonding network

with adsorbed water, and bulk water not shown in Fig. 3b for clarity. The Bader charge analysis of

Fig. S6 demonstrates that uncoordinated carbon of pristine g-C_5N_2 carriers a positive charge of 0.18 e

by average. This confirms that positively charged carbon of g-C_5N_2 interacts strongly with water

through its negatively charged oxygen atom.

The distributions of water near C and N sites are shown in Fig. 3c and 3d, respectively. In Fig. 3c, the first two peaks around 1.50 Å are from absorbed water. As illustrated in Fig. 3b, adsorbed water generally adopts the 'v' configuration, atop of C sites. Those adsorbed water still demonstrates a certain degree of freedom, which results in two close peaks at 1.50 Å. The peaks around 2.5 Å and 3.7 Å come from hydrogen-bonded water molecules. Limited by the pore size of g-C_5N_2, diameter ~13.82 Å, only two layers of hydrogen bonds (HB) are allowed, as illustrated by the dotted circles in Fig. 3b. The distribution analysis around N sites revealed one significant peak at around 2.97 Å, which represents hydrogen bonds between two adsorbed water molecules. Due to the negative charge, hydrogen of water stays closer to N sites, at 2.38 Å.
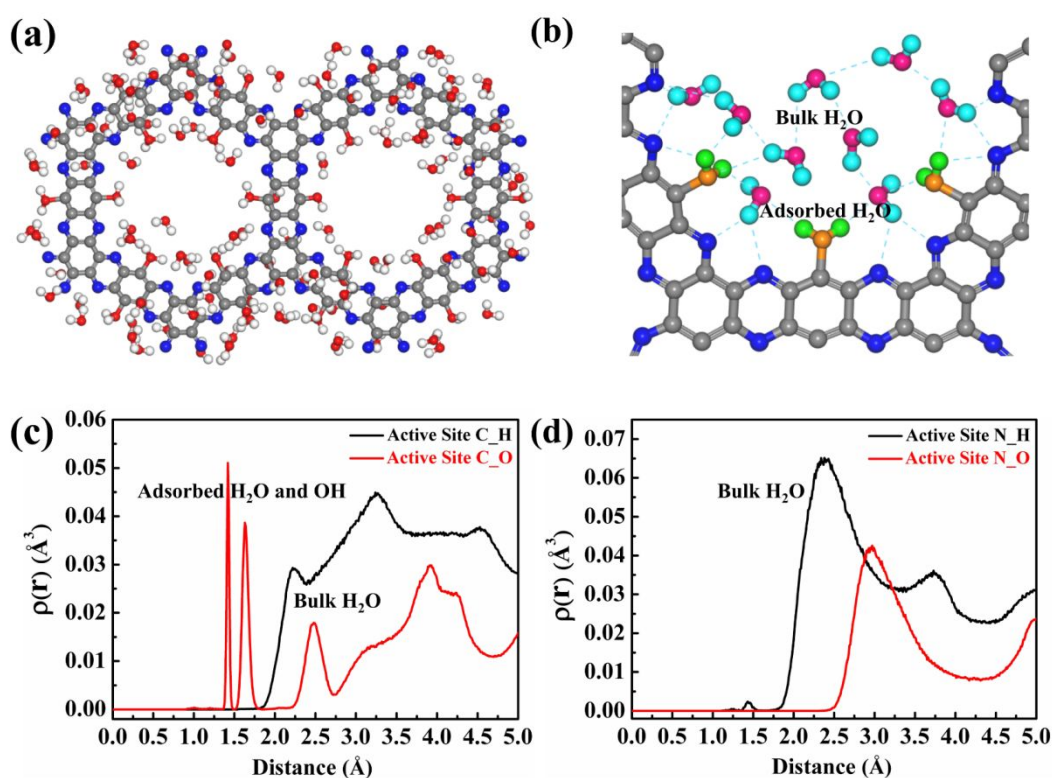

Fig. 3 (a) The distribution of water molecules in pores of dehydrogenated g-C_5N_2. (b) The distribution of water molecules, including adsorbed and bulk H_2O. The atomic density distribution for the water

molecule on (c) the C site on (d) the N site. The color codes are: C of g-C_5N_2, gray; N of g-C_5N_2, blue;

H of free H_2O, cyan; O of free H_2O, pink; H of adsorbed H_2O, green; O of adsorbed H_2O, yellow. Both

line and ball models are used in the snapshots, to emphasize the formation of H_2O_2. For clarity, not all

free water molecules are shown.

3.3 Reaction Mechanism for Direct H_2O_2 Synthesis

A series of RxMD and AIMD simulations have been performed to reveal the reaction mechanism

of H_2O and O_2 on g-C_5N_2 catalysts and the complete process of direct H_2O_2 synthesis. Fig. 4 presents

key snapshots of a representative RxMD simulation, demonstrating how one H_2O_2 molecule was

synthesized by a two-step reaction of H_2O/O_2 on the pristine g-C_5N_2 (Model 1). It is worth noting that

during the RxMD simulation, oxygen and hydrogen were assigned different colors to facilitate tracking

the reaction progress: adsorbed water, oxygen-yellow, hydrogen-green; near surface HB bonded water,

oxygen-pink, hydrogen-turquoise; gas-phase oxygen-red. As shown in Fig. 4, step 1 illustrates a

critical configuration where water molecules adsorbed at unsaturated C sites of the pore, and gas-phase

oxygen molecules were closer to adsorbed water. From step 1 to step 3, the interaction between O_2 and

adsorbed water was witnessed by the OH bond length, changing from 2.037 Å to 1.591 Å, and

eventually leading to the dissociation of the adsorbed water and the formation of the OOH*

intermediate.

Snapshots from step 4 to step 6 revealed an interesting proton exchange mechanism involving the

new generated OOH* intermediate, a nearby water molecule and another adsorbed water from the

neighboring C site. While the overall result is that one oxygen molecule interacts with two adsorbed

water to directly synthesize one H_2O_2 molecule, the snapshot of step 6 clearly shows that the two

hydrogen atoms of the H_2O_2 molecule came from two different proton donors, which is a convincing

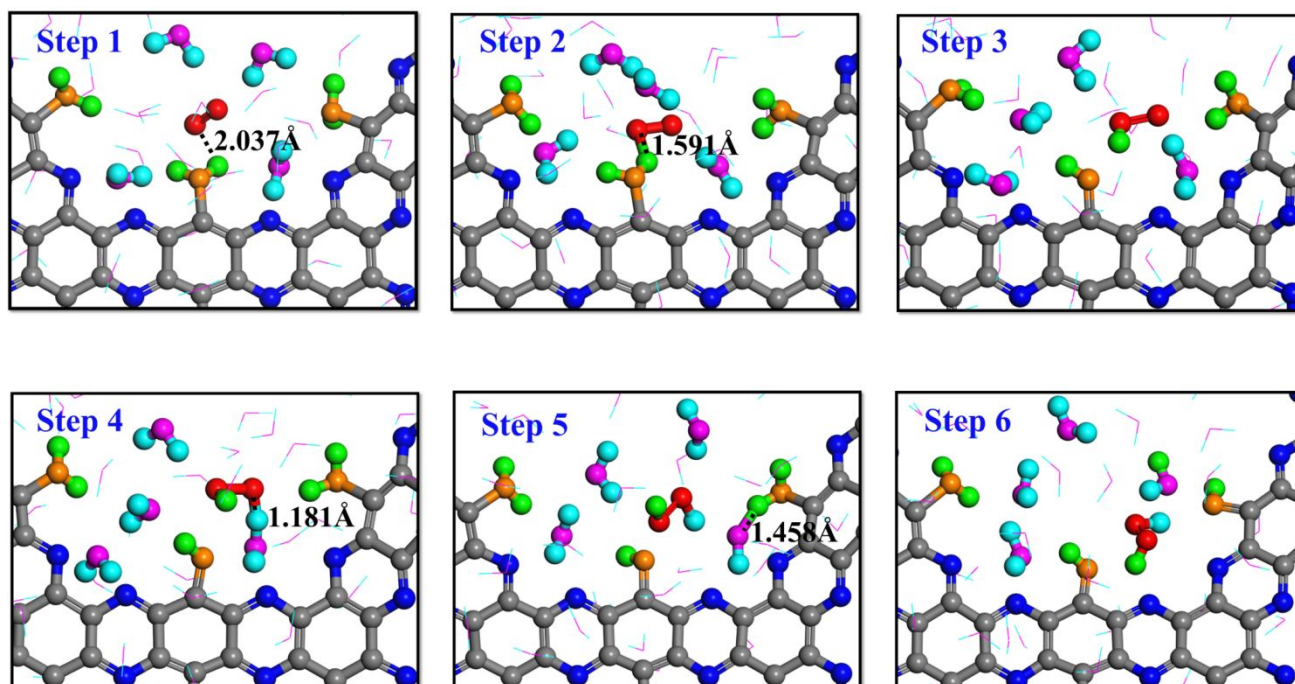evidence of the proton exchange event involving near surface water molecules.

Fig. 4 Proton transfer mechanism (PTM) on the dehydrogenated g-C_5N_2 system: the hydrogen atoms

of H_2O_2 come from adsorbed water and bulk water, respectively.

It is interesting to note that a different reaction mechanism was also observed from the simulation

trajectory, where the O_2 molecule interacted successively with two adsorbed H_2O molecules. As the

trajectory snapshots show in Fig. 5, the configuration of step 2 is critical: the O_2 molecule diffused to

the location where it could simultaneously interact with two adsorbed water. The HOO* intermediate

was then produced as a result of the interactions. In addition, since the intermediate was still very close

to the other adsorbed water, it could receive the second proton and lead the reaction to completion to

produce one H_2O_2 molecule. The color to hydrogen atoms of the H_2O_2, step 6 of Fig. 5, clearly

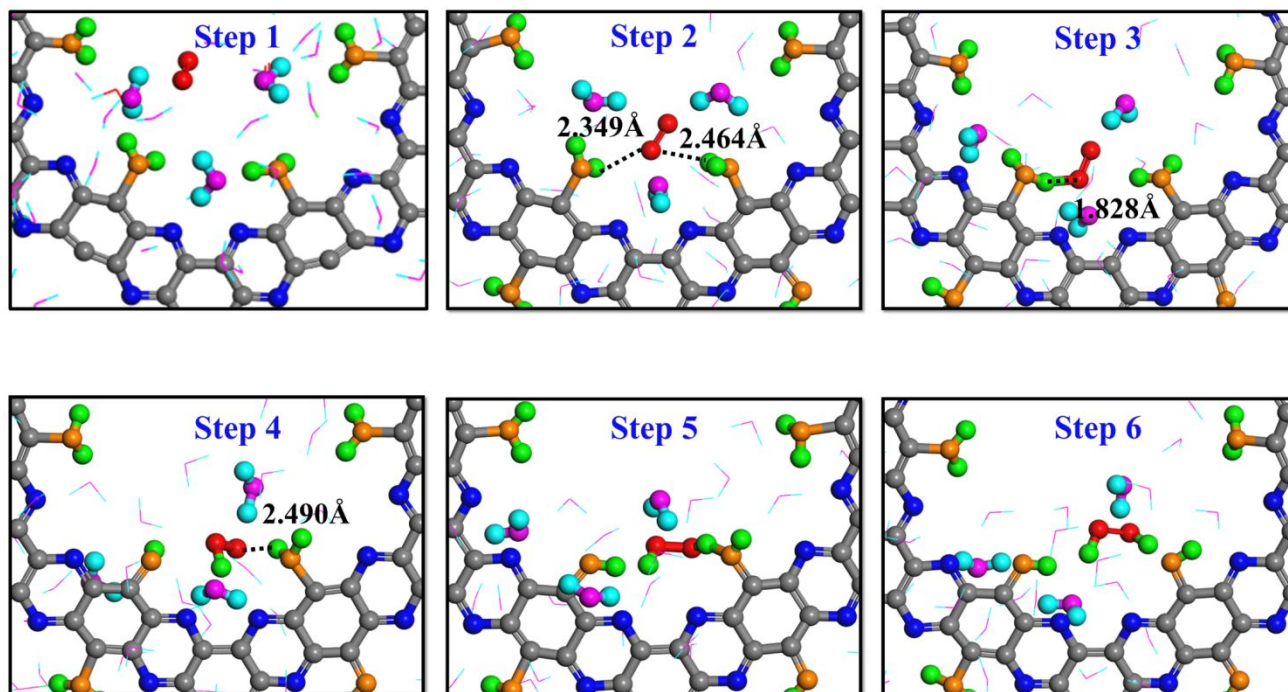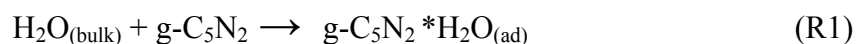demonstrates that no free or hydrogen bonded water participated in the two-step reaction process.

Fig. 5 Direct formation mechanism (DFM) dehydrogenated g-C_5N_2 system: the H atoms of H_2O_2

both come from adsorbed H_2O.

The snapshots shown in Fig. 6 are from the AIMD calculation of 5 O_2 molecules, 20 H_2O

molecules and a pristine g-C_5N_2 model. It is worth noting that, due to the expensive computational

cost, there were fewer oxygen and water molecules in the AIMD calculations. But both RxMD and

AIMD were performed at 300.0 K with the same g-C_5N_2 model. The analyses to AIMD and RxMD

trajectories come to the same conclusion, that is, the first critical step is H_2O adsorption at edge

unsaturated C sites, followed by O_2 interacting with adsorbed water to form HOO* intermediate. Then,

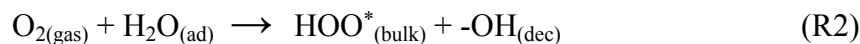different hydrogen suppliers can interact with HOO* to produce H_2O_2. Simultaneously, the interaction

between adsorbed water and nearby water molecules was also observed, sequentially producing a hydronium ion (H_3O^+, step 5) and then a Zundel cation ($H_5O_2^+$, step 6). The H_2O_2 was eventually synthesized as a reaction product between the HOO* and the $H_5O_2^+$, as illustrated by steps 8 and 9 of Fig. 6. As the reaction gone, the OH* or O* would be accumulated on the unsaturated edge-C sites. It is probably challenging to regenerate g-C_5N_2 by the H_2O/O_2 system as used in this work. However, convenient techniques are available to recycle the catalyst. Removing OH*/O* and regenerating active sites of carbon-based catalysts can be achieved by electrocatalytic reactions. For example, for the 4-electron ORR processes[63-65], adsorbed OH* is hydrogenated and removed in the form of H_2O. Liang and co-works studied the 4-electron ORR of nitrogen doptted graphene (N-graphene). Their results demonstrated that the removal of adsorbed OH* from N-graphene surface that is covered by O with a 1/6 monolayer surface oxygen coverage, has a small energy barrier of 0.32 eV in the water solution phase[66]. The regeneration depends closely on the form of deactivatd g-C_5N_2 catalysts, the concentration of H_3O^+ and the applied voltage. To validate the general regeneration process, a proof-of-concept calculation is designed in this work, to mimic a separate electrocatalytic treatement after the successful H_2O_2 production, to remove surface OH and O groups and regenerate active carbon sites of g-C_5N_2. As shown in Fig. S7(a), six H_2O and two H_3O^+ molecules are placed at the pore of the deactivated g-C_5N_2 where its edge nitrogen sites are fully hydrogenated and carbon sites are alternatively bonded with OH and O. The AIMD simulation results in Fig. S7 (b) and (c) show that within 0.2 ps, H_3O^+ interacts with oxygen-containing functional groups at edge carbon sites, transforming OH* and O* back to adsorbed water at edge carbon sites, thus regenerating the g-C_5N_2 catalyst for the next cycle of H_2O_2 production.

Both RxMD and AIMD reveal a same overall reaction mechanism which can be generally described by two sequential steps: (a) the formation of HOO* intermediates, from the interactions between oxygen and adsorbed water; (b) the completion of H_2O_2 synthesis, by the proton transfer between HOO* and chain-cluster water (or a second adsorbed water). (c) H_2O* regeneration, by interactions between residual OH* and H_3O^+ molecule. Key steps are summarized below:
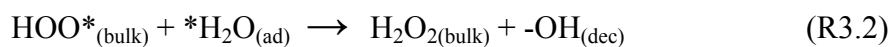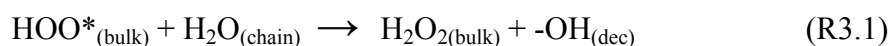
H_2O adsorption:

$$H_2O_{(bulk)} + g\text{-}C_5N_2 \longrightarrow g\text{-}C_5N_2 *H_2O_{(ad)} \qquad (R1)$$

HOO* formation:

$$O_{2(gas)} + H_2O_{(ad)} \longrightarrow HOO^*_{(bulk)} + \text{-}OH_{(dec)} \qquad (R2)$$

H_2O_2 formation:

$$HOO^*_{(bulk)} + H_2O_{(chain)} \longrightarrow H_2O_{2(bulk)} + \text{-}OH_{(dec)} \qquad (R3.1)$$

$$HOO^*_{(bulk)} + *H_2O_{(ad)} \longrightarrow H_2O_{2(bulk)} + \text{-}OH_{(dec)} \qquad (R3.2)$$

H_2O chain:

Hydronium ion: $*H_2O_{(ad)} + H_2O_{(bulk)} \longrightarrow H_3O^+_{(bulk)} + \text{-}OH_{(dec)} \qquad (R3.1a)$

Zundel cation: $H_3O^+_{(bulk)} + H_2O_{(bulk)} \longrightarrow H_5O_2^+_{(bulk)} \qquad (R3.1b)$

H_2O* regeneration: $OH* + H_3O^+_{(bulk)} \longrightarrow H_2O_{(ad)} + H_2O_{(bulk)} \qquad (R4)$
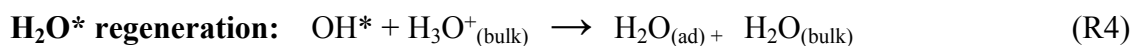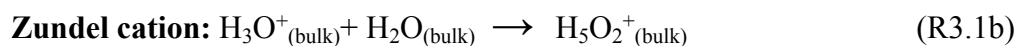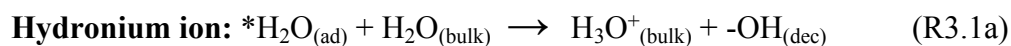
Fig. 6 Snapshots of H_2O_2 production on the dehydrogenated g-C_5N_2 described by the AIMD

simulations. Structures corresponding to the reaction path followed by PTM.

For other studied g-C_5N_2 models where N- or C- sites are hydrogenated, H_2O_2 was produced by a

similar reaction mechanism. The complete process was recorded for a few H_2O_2 molecules, as shown
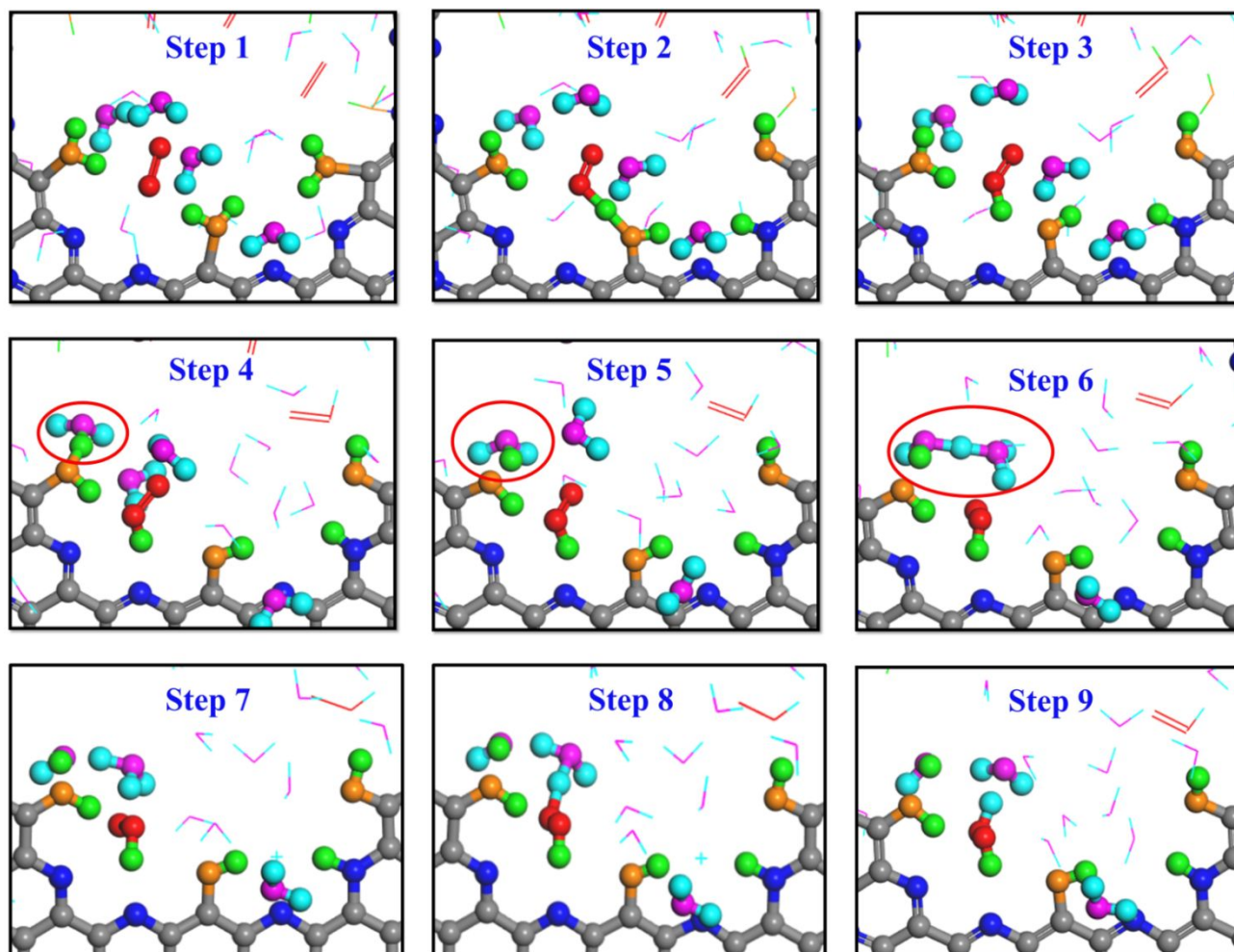
in Fig. S8-11. Hydrogenated N-sites (Model 3 and Model 4) are potential proton providers and it was

observed that: (a) H_2O_2 synthesized by interacting with an absorbed water and a hydrogenated N-site

(Model 3), Fig. S8; (b) H_2O_2 synthesized by directly interacting with two hydrogenated in the adsorbed

H_2O molecule (Model 3), Fig. S9 (c) H_2O_2 synthesized by interacting with an absorbed water and a hydrogenated N-site, via a H_2O proton transfer chain (Model 4), Fig. S10; (d) H_2O_2 synthesized by directly interacting with two hydrogenated N-sites (Model 4), Fig. S11. Krzysztof and co-workers[67] reported that the oxygen reduction proceeds through a one-step two-electron direct process with 2.15 eV energy barrier on the amino functionalized g-C_3N_4 structure. On the contrary, for the hydrogenated g-C_3N_4 catalyst, the two-step single-electron indirect H_2O_2 synthesis has an energy barrier of 1.78 eV. This indicates that O_2 molecule can directly interact with hydrogenated sites to produce H_2O_2.

Both RxMD and AIMD calculations confirm the direct H_2O_2 synthesis by chemisorbed water and gaseous colliding oxygen molecules, which is known as the Eley-Rideal (ER) reaction. A direct ER reaction is generally expected to occur only when there is a rather small activation barrier to the reaction, such as a gas-phase radical reactant which undergoes an exothermic reaction. In this work, we adopted CI-NEB method to study the reaction pathway and activation energy for producing HOO* intermediate and H_2O_2.
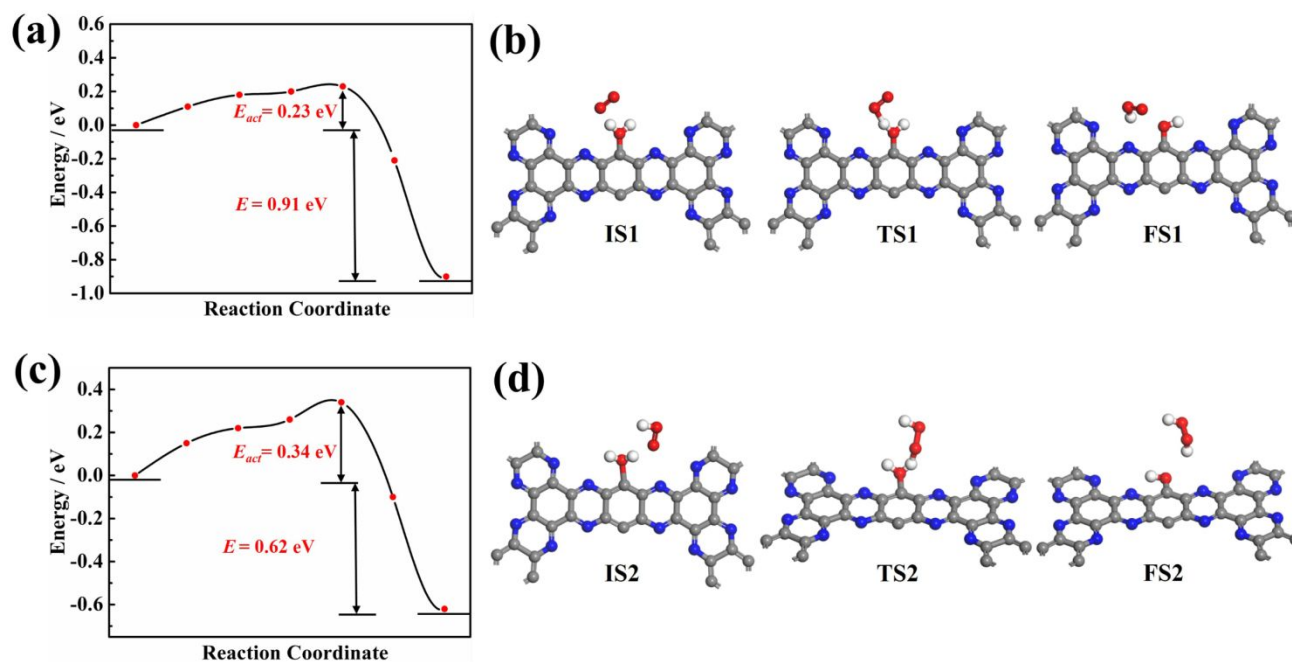
Fig. 7 Energy profile and optimized configurations for OOH* and H_2O_2 formation. (a), (c) Energy profile for OOH* and H_2O_2 formation by DFT calculation, respectively; (b), (d) The optimized initial state, transition state and final state configurations for OOH* and H_2O_2 formation, respectively.

As shown in Fig. 7a, for the HOO* intermediate, the initial configuration in the system has a gaseous O_2 and one adsorbed H_2O at g-C_5N_2. While the final configuration has a HOO* intermediate and an OH-functionalized g-C_5N_2. For the initial configuration, upon water adsorption at the unsaturated C sites, the O-H bond was elongated, changing from 0.972 Å of the bulk to 1.110 Å. The transition state was identified in which the gaseous O_2 was interacting with the adsorbed water, to the extent that the adsorbed water has two equally elongated O-H bonds, one with the oxygen of the gaseous O_2, the other from the adsorbed water. The calculation revealed that the activation energy (E_{act}) to HOO* formation was 0.23 eV, and the overall reaction was exothermic, releasing 0.91 eV

from the system. The exothermic nature indicates that the proton transfer from adsorbed water to a nearby O_2 molecule is energetically favored.

Fig. 7b shows the reaction pathway of how the HOO* intermediate received the second proton to generate a H_2O_2 molecule. As revealed by RxMD and AIMD calculations, this reaction generally involves 'free' water molecules to transfer protons from adsorbed water. It was also observed, see Fig. 5, that the gaseous O_2 could interact successively with two adsorbed H_2O molecules to produce a H_2O_2 molecule, which does not require much diffusion of the HOO* intermediate. It is also worth pointing out that there is no 'free' water considered in the CI-NEB calculations, only the direct reaction between HOO* and adsorbed water to H_2O_2 was calculated. The result suggested that a larger activation energy (0.34 eV) was necessary to overcome the reaction barrier. But the overall reaction was also exothermic, discharging 0.63 eV from the system.

3.4 Proton Transfer along Hydrogen Bonds

Proton transfer is essential to many aqueous processes, from ion channel function to enzymatic reactions[68-70]. Especially for photocatalytic[71, 72] and electrocatalytic reactions[73, 74], simultaneous gain or lose electrons and protons are frequently happening in aqueous solutions. Nevertheless, not enough emphasis has been placed on the effect of proton transfer for aqueous reactions. Experimentally, direct observation of proton transfer is challenging due to the short lifetime of intermediates and the difficulty of distinguishing proton, electron and their coupling with solvent molecules. For example, Yu and co-workers[75] investigated the Langmuir-Hinshelwood (LH) and ER mechanisms for the ORR on graphene

sheets. They performed *ab initio* DFT calculations to mimic ER reactions under an alkaline environment, with H shuttling through one or two water molecules. Other theoretical efforts of understanding proton transfer mechanisms have been summarized in recent reviews[76-85]. It has been demonstrated that the proton transfer can largely determine the energetic profile and reaction pathway. However, as far as we are aware of, there is no quantitative description of proton transfer in ORR processes
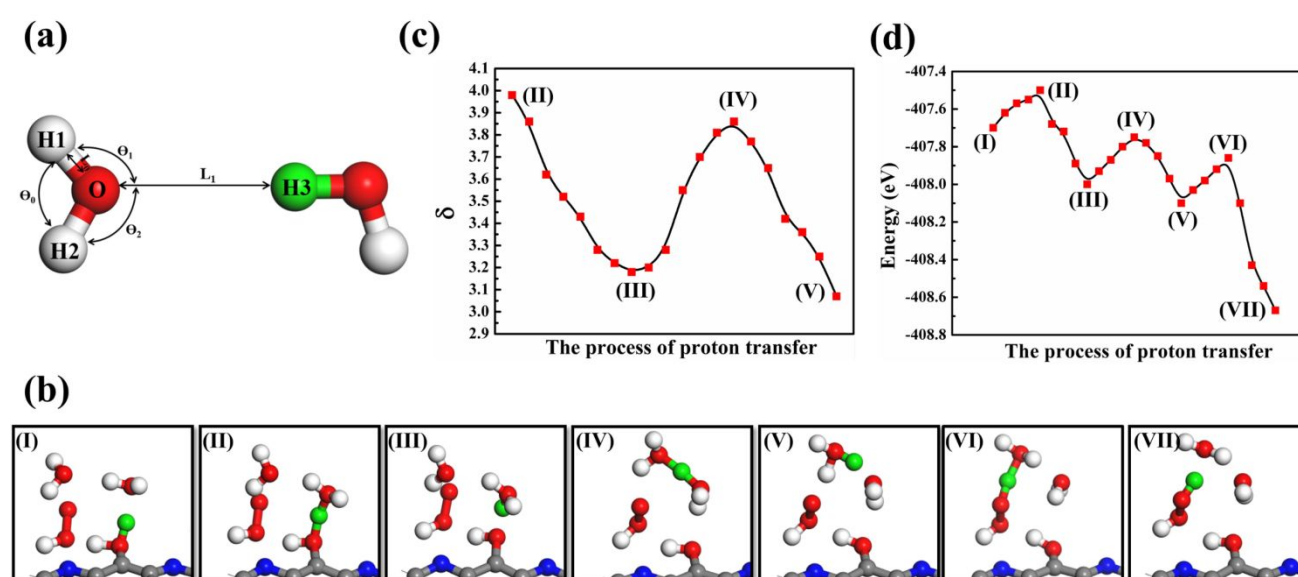
Fig. 8 Proton transfer via a chain of water molecules. (a) Schematic representation of the proton transfer process. (b) Trajectory snapshots (I-VII) of critical configurations to the proton transfer for H_2O_2 production. (c), (d) The change of φ and the total energy in the process of proton transfer, respectively. The dissociated proton exists as a Zundel ion and a hydrated hydronium ion in the systems. C, O, H and N atoms are colored gray, red, white and blue, respectively. H atom of the adsorbed water that participates the proton transfer is colored green to guide the viewing.

Here, we propose a proton transfer descriptor based on structural information of involved water molecules. As illustrated in Fig. 8a, the descriptor δ describes the geometric requirement, assuming proton transfer happens when oxygen atoms of water molecules have three identical hydrogen atoms nearby. Therefore, breaking O-H bonds and exchanging hydrogen atoms (protons) require a negligible energy penalty. The δ value is estimated by the equation:

$$\delta = \frac{\theta_1}{\theta_0} + \frac{\theta_2}{\theta_0} + \frac{L_1}{L_0}$$

where θ_0 and L_0 are respectively equilibrium angle and bond length of free H_2O molecules; θ_1 and θ_2 are the new angles, namely H1-O-H3, H2-O-H3 according to Fig. 8a, formed between two nearby water molecules; L_1 is the distance between oxygen atom and the potential exchangeable H3 hydrogen (proton). Mathematically, δ reaches a minimum whenever there is a proton transfer event.

Previous studies observed Eigen $(H_9O_4^+)$[86, 87] and $H_5O_2^{+}$[88] from bulk water. This suggests that proton transfer events involving two or three water molecules are energetically favorable. In this work, dehydrogenated carbon sites provide localized positive charge centers, which promote H_2O adsorption and subsequent $H_5O_2^+$ ion formation (Fig. 8b). Representative snapshots in Fig.8b demonstrate how near-surface water molecules participate in proton transfer events and promote the HOO* intermediate to receive a proton and thus produce H_2O_2. The AIMD trajectory reveals that two bulk water molecules are involved in this proton transfer process (Fig. 8b (I)): firstly, as shown in Fig. 8b (II), the adsorbed H_2O interacted with a nearby bulk H_2O to form a hydronium H_3O^+ and an OH functional group of g-C_5N_2, after that adsorbed water gave up the proton (green color), see Fig. 8b (III). The hydronium

H_3O^+ then interacted with another bulk water molecule to form $H_5O_2^+$ cation, shown in Fig. 8b (IV). It is worth noting that the oxygen-oxygen distance, between the second bulk water and the previously formed H_3O^+, is about 2.70 Å which is within a typical hydrogen bond cutoff[89]. This suggests that the second water could easily accept a hydrogen from the H_3O^+, forming a new hydronium H_3O^+, see Fig. 8b (V). Since the new H_3O^+ was much closer to the HOO* intermediate, it easily gives up a proton to HOO* to promote the formation of H_2O_2 (Fig. 8b (VI-VII)). Additionally, direct proton exchange was also observed between adsorbed H_2O molecules and g-C_5N_2, see Fig. S12.

It has been reported[89] that a Zundel proton is formed when two water molecules, the oxygen-oxygen distance, are within 1.35 Å. To quantify proton transfer events, we adopted the same cut-off of 1.35 Å to determine whether a proton transfer event could happen between two water. In addition, since the four atoms of hydronium ion H_3O^+ adopts a trigonal pyramidal geometry, an angular term is necessary to describe proton transfer events. Using the definition of φ, the dynamics trajectory was monitored. As shown in Fig. 8b, in the process of forming the first H_3O^+, the value of the bulk and adsorbed H_2O molecules gradually decreases (II to III), eventually reaching the minimum where the bulk water molecule accepted a proton from the adsorbed water, forming the H_3O^+. From III to IV of Fig. 8b, the H_3O^+ interacted with a second water, firstly forming the Zundel proton $H_5O_2^+$, where increased to reach the maximum at IV. The value then decreased and reached the minimum again, where the $H_5O_2^+$ decomposed to a new H_3O^+. The function is similar to the double-minimum potentials that are often used to describe hydrogen bonds and can provide a handy description of proton transfer dynamics. In addition, to better interpret the proton transfer and the H_2O_2

formation, energetics information to each snapshot has been calculated via ab initio DFT. As shown

in the Fig 8d, three energy barriers were identified to one successful proton transfer and one HOO

hydrogenation. The energy barrier of forming the first and second H_3O^+ is 0.20 eV and 0.25 eV (Fig.8d

(I-V)), respectively. More importantly, the *HOO only needed to overcome a barrier of 0.24 eV to

form the H_2O_2 by proton transfer.

3.5 H_2O_2 Evolution on Different g-C_5N_2 Surface

Aforementioned results have clearly demonstrated that pristine dehydrogenated g-C_5N_2 is

effective to catalyze H_2O/O_2 reaction and produce H_2O_2. The two-step reaction mechanism depends

critially on both adsorbed water (at unsaturated C sites) and free water (near the pores of g-C_5N_2). It is

important to evaluate the catalytic performance of other models where C and N sites are particially or

fully hydrogenated. Similar to Sec. 2.1, 500 H_2O and 25 O_2 molecules were randomly placed on both

sides of the g-C_5N_2 model, of the size 68.98 Å (y) × 57.71 Å (x). RxMD calculations were performed

at 300.0 K for all five models and the results are shown in Fig. 9a. Firstly, g-C_5N_2 shows a general

catalytic activity to H_2O/O_2 reactions that H_2O_2 was produced from all five systems. The best yield

(eight H_2O_2) was from the pristine g-C_5N_2 (Model 1, no hydrogenation). And two different types of

H_2O_2 molecule were synthesized from different hydrogen resources, see the Fig. 9c. This phenomenon

was also observed in AIMD simulations of Model 3 (Fig. S8-9) and Model 4 (Fig. S10-11). However,

the only five H_2O_2 molecules were produced in the Model 3 where the C-site no hydrogenation and N

sites are fully hydrogenated. The following two observations could explain this result: (a) the transition state calculation indicated that the activation energy of O_2 reacting with H of the edge-N-H species is 0.58 eV (Fig S14 (a)), which is higher than that of O_2 reacting with adsorbed water at the edge C sites. The activation energy to HOO* and H_2O_2 formation only was respectively 0.23 eV and 0.32 eV for Model 1. Thus, O_2 shall preferentially interact with the adsorbed H_2O. (b) As shown in the Fig S8, AIMD calculations reveal that when adsorbed H_2O of edge C sites and hydrogenated H of edge N sites coexist, O_2 preferentially reacted with adsorbed H_2O to form HOO* intermediates. Those HOO* could then capture H from those edge N sites to form H_2O_2. Based on those observations, we conclude that O_2 reacting with two adsorbed water molecules, as shown for Model 1, is energetically favored and that Model 1 is more active than Mode 3 for the studied H_2O_2 synthesis.

For Model 2(C-site fully hydrogenated), Model 4(C-site and N-site fully hydrogenated) and Model 5 (the most stable model, with C sites fully and N sites partially hydrogenated), the yield is relatively lower, only 1, 3 and 2 H_2O_2 molecules were produced respectively during the simulation of 1000 ps. According to AIMD results, O_2 can only capture protons from the hydrogenated N sites due to the very stable C-H bonds. In addition, adsorption configurations of H_2O and O_2 on Model 5 have been optimized via *ab initio* DFT calculations based on the Bader charge analysis (Fig. S13a). The adsorption energy of O_2 is -0.95 eV (Fig. S13b), and that of H_2O is only -0.05 eV (Fig. S13c). Stronger O_2 adsorption can significantly weaken the bonding energy of O_2, which will reduce the selectivity of H_2O_2 and produce water as a side reaction product. Thus, the number of formed H_2O_2 of Model 4 are more than Models 2 and Model 5 with all the edge-C hydrogenated.

Although the Gibbs free energy was calculated to evaluate possible g-C_5N_2 hydrogenations, other factors, such as defects and solutions, could also affect the stability and reactivity of g-C_5N_2 catalysts. If one only considers the best reactivity, as shown in Fig. 9a, the pristine g-C_5N_2, neither edge nitrogen nor carbon sites are hydrogenated, demonstrates the best catalytic performance. While the most stable g-C_5N_2 model (Model 5) has a relatively poor catalytic performance to H_2O_2 synthesis. The activity is the major contributor to H_2O_2 synthesis, but the successful application of g-C_5N_2 materials shall also depend strongly on the stability. Regardless of mechanism or yield of H_2O_2 formation analysis, both suggest that unsaturated edge carbon sites do not promote immediate water dissociation and could be reactivated afterwards. We expect that those unsaturated edge sites are available both from the synthesized g-C_5N_2 and during the process of catalyzing H_2O/O_2 reactions.
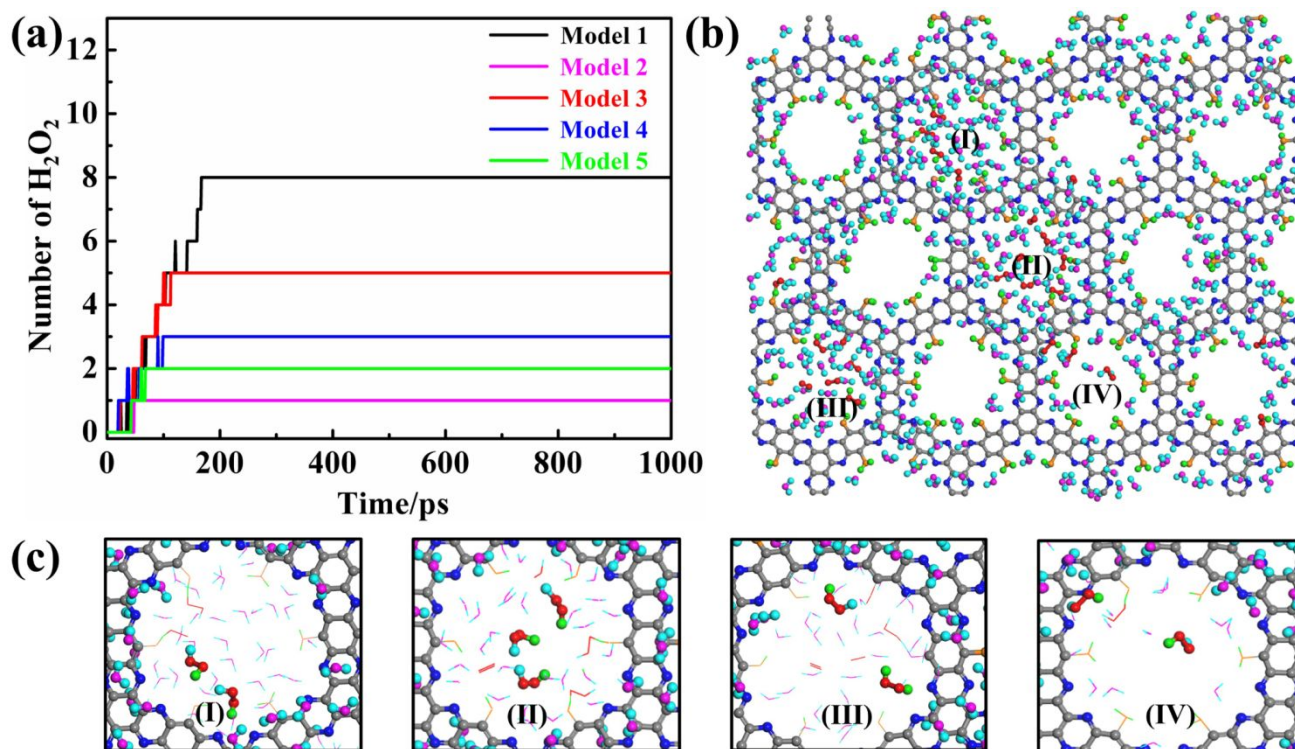
Fig. 9 RxMD simulations of H_2O_2 synthesis on five g-C_5N_2 models at 300.0 K. (a) the number of H_2O_2 molecules produced as a function of simulation time. (b) Snapshots of H_2O and O_2 at dehydrogenated g-C_5N_2 phase surface described by the RxMD simulations at 200.0 ps. (c) Observed H_2O_2 production from different nanopores of Model 1 as highlighted in (b).

4. Conclusion

In summary, this work represents a computational study of direct H_2O_2 synthesis from H_2O and O_2 on a metal-free porous graphitic carbon nitride catalyst. Through a combination of *ab initio* molecular dynamics simulation, reactive molecular dynamics (RxMD) calculation, and the *ab inito* density functional theory based thermodynamics approach, g-C_5N_2 models with different hydrogenation have been examined to catalyze H_2O/O_2 reactions for H_2O_2 production. The Gibbs free energy calculation and the thermal stability discussion of various g-C_5N_2 models could be a general protocol to screen and evaluate carbon-based materials which are doped by a wide range of other elements. The two-step reaction mechanism has been elucidated, which invloves sequentally the adsorption and activation of water at unsaturated C sites of g-C_5N_2, producing HOO* intermediates, and synergetic proton transfers to promote HOO*-to-H_2O_2 reactions, via clusters of free and adsorbed water. Other fundamental facts include that a pristine g-C_5N_2 is the most active catalyst, and that a preferential water adsorption (instead of oxygen adsorption) on g-C_5N_2 is critical to direct H_2O_2 synthesis. Future development of new catalysts could take this as a general criterion to design reactive sites and optimize catalyst geometry, to simultaneously favor water activation at reactive sites and

water-chain assisted fast proton transfer processes. This work paves the way for using carbon-based sustainable catalysts for direct H_2O_2 synthesis via the water/oxygen promising strategy. In addition, the fundamental insight could also shed light on selecting and designing other green catalysts for heterogeneous oxygen hydrogenation reactions.

Additional information

Supplementary information accompanies this paper is available free of charge from the publisher.

Acknowledgments

Competing financial interests

The authors declare no competing financial interests.

References

1.   J. M. Campos-Martin, G. Blanco-Brieva and J. L. G. Fierro, *Angew. Chem. Int. Ed.*, 2006, **45**, 6962-6984.

2.   E. Brillas, Sires, I. & Oturan, M. A, *Chem. Rev.*, 2009, **109**, 6570-6631.

3.   N. Agarwal, Freakley, S. J., McVicker, R. U., Althahban, S. M. & Dimitratos, N, *Science.*, 2017, **358**, 223-227.

4.   Y. Yi, L. Wang, G. Li and H. Guo, *Catal. Sci. Technol.*, 2016, **6**, 1593-1610.

5.   J. Garcia-Serna, T. Moreno, P. Biasi, M. J. Cocero, J. P. Mikkola and T. O. Salmi, *Green Chem.*, 2014, **16**, 2320-2343.

6.   J. K. Edwards, B. Solsona, E. N. N, A. F. Carley, A. A. Herzing, C. J. Kiely and G. J. Hutchings, *Science.*, 2009, **323**, 1037-1041.

7.   Q. Liu, J. C. Bauer, R. E. Schaak and J. H. Lunsford, *Angew. Chem. Int. Ed.*, 2008, **47**, 6221-6224.

8.   G. M. Lari, B. Puertolas, M. Shahrokhi, N. Lopez and J. Perez-Ramirez, *Angew. Chem. Int. Ed*, 2017, **56**, 1775-1779.

9.   J. S. Jirkovský, I. Panas, E. Ahlberg, M. Halasa, S. Romani and D. J. Schiffrin, *J. Am. Chem. Soc.*, 2011, **133**, 19432-19441.

10.   I. Kim, M.-g. Seo, C. Choi, J. S. Kim, E. Jung, G.-H. Han, J.-C. Lee, S. S. Han, J.-P. Ahn, Y. Jung, K.-Y. Lee and T. Yu, *ACS Appli Mater Inter.*, 2018, **10**, 38109-38116.

11.   E. Pizzutilo, S. J. Freakley, S. Cherevko, S. Venkatesan, G. J. Hutchings, C. H. Liebscher, G. Dehm and K. J. J. Mayrhofer, *ACS Catal.*, 2017, **7**, 5699-5705.

12.   Y. Shiraishi, Y. Kofuji, H. Sakamoto, S. Tanaka, S. Ichikawa and T. Hirai, *ACS Catal*, 2015, **5**, 3058-3066.

13.   Y. Isaka, Y. Kawase, Y. Kuwahara, K. Mori and H. Yamashita, *Angew. Chem. Int. Ed.*, 2019, **58**, 5402-5406.

14.   S. Zhao, T. Guo, X. Li, T. Xu, B. Yang and X. Zhao, *Appl. Cataly B Environ.*, 2018, **224**, 725-732.

15.   M. Gryszel, A. Markov, M. Vagin and E. D. Głowacki, *J. Mater. Chem. A*, 2018, **6**, 24709-24716.

16.   X. Shi, S. Siahrostami, G.-L. Li, Y. Zhang, P. Chakthranont, F. Studt, T. F. Jaramillo, X. Zheng and J. K. Nørskov, *Nat. Commun*, 2017, **8**, 701.

17. S. Siahrostami, A. Verdaguer-Casadevall, M. Karamad, D. Deiana, P. Malacrida, B. Wickman, M. Escudero-Escribano, E. A. Paoli, R. Frydendal, T. W. Hansen, I. Chorkendorff, I. E. L. Stephens and J. Rossmeisl, *Nat. Mater*, 2013, **12**, 1137-1143.

18. S. Kato, J. Jung, T. Suenobu and S. Fukuzumi, *Energy. Environ. Sci*, 2013, **6**, 3756.

19. Y. T. Ichiro, M., *Angew. Chem. Int. Ed.*, 2008, **47**, 1900-1902.

20. H. Jing, Q. F. Zhang, N. Large, C. M. Yu, D. A. Blom, P. Nordlander and H. Wang, *Nano Lett.*, 2014, **14**, 3674-3682.

21. C. H. Choi, H. C. Kwon, S. Yook, H. Shin, H. Kim and M. Choi, *J. Phys. Chem. C*, 2014, **118**, 30063-30070.

22. S. Yang, J. Kim, Y. J. Tak, A. Soon and H. Lee, *Angew. Chem. Int. Ed.*, 2016, **55**, 2058-2062.

23. W. R. P. Barros, Q. L. Wei, G. X. Zhang, S. H. Sun, M. R. V. Lanza and A. C. Tavares, *Electrochim. Acta*, 2015, **162**, 263-270.

24. M. B. Zakaria, C. Li, M. Pramanik, Y. Tsujimoto, M. Hu, V. Malgras, S. Tominaka and Y. Yamauchi, *J. Mater. Chem. A*, 2016, **4**, 9266-9274.

25. S. Chen, Z. Chen, S. Siahrostami, D. Higgins, D. Nordlund, D. Sokaras, T. R. Kim, Y. Liu, X. Yan, E. Nilsson, R. Sinclair, J. K. Nørskov, T. F. Jaramillo and Z. Bao, *J. Am. Chem. Soc.* , 2018, **140**, 7851-7859.

26. T.-P. Fellinger, F. Hasché, P. Strasser and M. Antonietti, *J. Am. Chem. Soc.*, 2012, **134**, 4072-4075.

27. L. Han, Y. Sun, S. Li, C. Cheng, C. E. Halbig, P. Feicht, J. L. Hübner, P. Strasser and S. Eigler, *ACS Catal*, 2019, **9**, 1283-1288.

28. J. Park, Y. Nabae, T. Hayakawa and M. a. Kakimoto, *ACS Catal.*, 2014, **4**, 3749-3754.

29. Y. Cao, S. Deng, Q. Fang, X. Sun, C. Zhao, J. Zheng, Y. Gao, H. Zhuo, Y. Li, Z. Yao, Z. Wei, X. Zhong, G. Zhuang and J. Wang, *Nanotechnology*, 2019, **30**, 335403.

30. K. Gong, F. Du, Z. Xia, M. Durstock and L. Dai, *Science*, 2009, **323**, 760-764.

31. Z. Pan, K. Wang, Y. Wang, P. Tsiakaras and S. Song, *Appl. Cataly B Environ.*, 2018, **237**, 392-400.

32. L. Tao, Q. Wang, S. Dou, Z. Ma, J. Huo, S. Wang and L. Dai, *Chem. Commun.*, 2016, **52**, 2764-2767.

33. P. Zhang, D. Sun, A. Cho, S. Weon, S. Lee, J. Lee, J. W. Han, D.-P. Kim and W. Choi, *Nat. Commun*, 2019, **10**, 940.

34. Z. Lu, G. Chen, S. Siahrostami, Z. Chen, K. Liu, J. Xie, L. Liao, T. Wu, D. Lin, Y. Liu, T. F. Jaramillo, J. K. Norskov and Y. Cui, *Nat. Catal*, 2018, **1**, 156-162.

35. H. W. Kim, M. B. Ross, N. Kornienko, L. Zhang, J. Guo, P. Yang and B. D. McCloskey, *Nat. Catal.*, 2018, **1**, 282-290.

36. V. Briega-Martos, A. Ferre-Vilaplana, A. de la Peña, J. L. Segura, F. Zamora, J. M. Feliu and E. Herrero, *ACS Catal*, 2016, **7**, 1015-1024.

37. Y. Kou, Y. Xu, Z. Guo and D. Jiang, *Angew. Chem. Int. Ed.*, 2011, **50**, 8753-8757.

38. Z.-D. Yang, W. Wu and X. C. Zeng, *J. Mater. Chem. C*, 2014, **2**, 2902-2907.

39. A. C. T. van Duin, S. Dasgupta, F. Lorant and W. A. Goddard, *J. Phys. Chem. A*, 2001, **105**, 9396-9409.

40. K. Chenoweth, A. C. T. van Duin and W. A. Goddard, III, *J. Phys. Chem. A*, 2008, **112**, 1040-1053.

41. L. L. Huang, M. Seredych, T. J. Bandosz, A. C. T. van Duin, X. H. Lu and K. E. Gubbins, *J. Chem. Phys.*, 2013, **139**, 194707.

42. S. Plimpton, *J. Comput. Phys.*, 1995, **117**, 1-19.

43. S. Nose, *J. Chem. Phys.*, 1984, **81**, 511-519.

44. W. G. Hoover, *Phys. Rev. A, Gen. Phys.*, 1985, **31**, 1695-1697.

45. L. Verlet, *Phys. Rev.*, 1967, **159**, 98-103.

46. P. E. Blochl, *Phys. Rev. B*, 1994, **50**, 17953-17979.

47. G. Kresse and J. Furthmuller, *Comput. Mater. Sci.*, 1996, **6**, 15-50.

48. G. Kresse and D. Joubert, *Phys. Rev. B.*, 1999, **59**, 1758-1775.

49. J. P. Perdew, K. Burke and M. Ernzerhof, *Phys. Rev. Lett.*, 1996, **77**, 3865-3868.

50. S. Grimme, J. Antony, S. Ehrlich and H. Krieg, *J. Chem. Phys.*, 2010, **132**, 154104.

51. R. A. Evarestov and V. P. Smirnov, *Phys. Rev. B.*, 2004, **70**, 233101.

52.   G. Henkelman, B. P. Uberuaga and H. Jonsson, *J. Chem. Phys.*, 2000, **113**, 9901-9904.

53.   J. VandeVondele, M. Krack, F. Mohamed, M. Parrinello, T. Chassaing and J. Hutter, *Comput. Phys. Commun.*, 2005, **167**, 103-128.

54.   W. G. Hoover, *Phys. Rev. A, Gen. Phys.*, 1985, **31**, 1695-1697.

55.   J. VandeVondele and J. Hutter, *J. Chem. Phys.*, 2007, **127**, 114105.

56.   G. Lippert, J. Hutter and M. Parrinello, *Mol. Phys.*, 1997, **92**, 477-487.

57.   F. Bottin, F. Finocchi and C. Noguera, *Phys. Rev. B*, 2003, **68**, 13.

58.   E. Heifets, S. Piskunov, E. A. Kotomin, Y. F. Zhukovskii and D. E. Ellis, *Phys. Rev. B*, 2007, **75**, 13.

59.   Q. Cai, J.-g. Wang, Y. Wang and D. Mei, *J. Phys. Chem. C.*, 2016, **120**, 19087-19096.

60.   D. Gao, H. Zhou, F. Cai, D. Wang, Y. Hu, B. Jiang, W.-B. Cai, X. Chen, R. Si, F. Yang, S. Miao, J. Wang, G. Wang and X. Bao, *Nano. Res.*, 2017, **10**, 2181-2191.

61.   K. Reuter and M. Scheffler, *Phys. Rev. B.*, 2003, **68**, 045407.

62.   Http://Webbook.Nist.Gov/Chemistry. *Chemistry WebBook. National Institute of Standards and Technology: Gaithersburg, MD*, 2003, **69**.

63.   R. Cao, J.-S. Lee, M. Liu and J. Cho, *Advanced Energy Materials*, 2012, **2**, 816-829.

64.   Z. L. Wang, D. Xu, J. J. Xu and X. B. Zhang, *Chem. Soc. Rev.*, 2014, **43**, 7746-7786.

65.   R. Ma, G. Lin, Y. Zhou, Q. Liu, T. Zhang, G. Shan, M. Yang and J. Wang, *npj Computational Materials*, 2019, **5**, 78.

66.   L. Yu, X. Pan, X. Cao, P. Hu and X. Bao, *J. Catal.*, 2011, **282**, 183-190.

67.   J. Goclon and K. Winkler, *Appl. Surf. Sci.*, 2018, **462**, 134-141.

68.   O. Gerlits, T. Wymore, A. Das, C. H. Shen, J. M. Parks, J. C. Smith, K. L. Weiss, D. A. Keen, M. P. Blakeley, J. M. Louis, P. Langan, I. T. Weber and A. Kovalevsky, *Angew. Chem. Int. Ed.*, 2016, **55**, 4924-4927.

69.   C. T. Supuran, *Biochem. J*, 2016, **473**, 2023-2032.

70.   E. Nango, A. Royant, M. Kubo, T. Nakane, C. Wickstrand, T. Kimura, T. Tanaka, K. Tono, C. Y. Song, R. Tanaka, T. Arima, A. Yamashita, J. Kobayashi, T. Hosaka, E. Mizohata, P. Nogly, M. Sugahara, D. Nam, T. Nomura, T. Shimamura, D. Im, T. Fujiwara, Y. Yamanaka, B. Jeon,

T. Nishizawa, K. Oda, M. Fukuda, R. Andersson, P. Bath, R. Dods, J. Davidsson, S. Matsuoka, S. Kawatake, M. Murata, O. Nureki, S. Owada, T. Kameshima, T. Hatsui, Y. Joti, G. Schertler, M. Yabashi, A. N. Bondar, J. Standfuss, R. Neutze and S. Iwata, *Science*, 2016, **354**, 1552-1557.

71.   C. Chen, T. Shi, W. Chang and J. Zhao, *ChemCatChem*, 2015, **7**, 724-731.

72.   K. Yamamoto and K. Takatsuka, *Physi. Chem. Chem. Phys.*, 2018, **20**, 6708-6725.

73.   A. Badalyan and S. S. Stahl, *Nature*, 2016, **535**, 406-410.

74.   C. W. Lee, J. S. Hong, K. D. Yang, K. Jin, J. H. Lee, H.-Y. Ahn, H. Seo, N.-E. Sung and K. T. Nam, *ACS Catal.*, 2018, **8**, 931-937.

75.   Q. Ly, B. V. Merinov, H. Xiao, W. A. Goddard and T. H. Yu, *J. Phys. Chem. C.*, 2017, **121**, 24408-24417.

76.   M. T. M. Koper, *Chem. Sci.*, 2013, **4**, 2710-2723.

77.   U. W. Schmitt and G. A. Voth, *J. Chem. Phys*, 1999, **111**, 9361-9381.

78.   S. Hammes-Schiffer, *Acc. Chem. Res.*, 2001, **34**, 273-281.

79.   J. M. Saveant, *Acc. Chem. Res.*, 1993, **26**, 455-461.

80.   S. Scheiner, *Acc. Chem. Res*, 1985, **18**, 174-180.

81.   M. H. V. Huynh and T. J. Meyer, *Chem. Rev.*, 2007, **107**, 5004-5064.

82.   D. R. Weinberg, C. J. Gagliardi, J. F. Hull, C. F. Murphy, C. A. Kent, B. C. Westlake, A. Paul, D. H. Ess, D. G. McCafferty and T. J. Meyer, *Chem. Rev*, 2012, **112**, 4016-4093.

83.   R. I. Cukier and D. G. Nocera, *Annu. Rev. Phys. Chem*, 1998, **49**, 337-369.

84.   J. M. Mayer, *Annu. Rev. Phys. Chem.*, 2004, **55**, 363-390.

85.   S. Hammes-Schiffer and A. A. Stuchebrukhov, *Chem. Rev.*, 2010, **110**, 6939-6960.

86.   M. Eigen, *Angew. Chem.*, 1963, **75**, 489-508.

87.   M. Eigen, *Angew. Chem. Int. Ed.*, 1964, **3**, 1-72.

88.   G. Zundel, *Adv. Chem. Phys.*, 2000, **111**, 1-217.

89.   D. Marx, *ChemPhysChem*, 2006, **7**, 1848-1870.